

QDFlow: A Python package for physics simulations of quantum dot devices

Donovan L. Buterakos^{1,2*}, Sandesh S. Kalantre^{1,2,4}, Joshua Ziegler²,
Jacob M Taylor^{1,2,3,5} and Justyna P. Zwolak^{1,2,3†}

1 Joint Center for Quantum Information and Computer Science, University of Maryland,
College Park, MD 20742, USA

2 National Institute of Standards and Technology, Gaithersburg, MD 20899, USA

3 Department of Physics, University of Maryland, College Park, MD 20742, USA

4 Department of Physics, Stanford University, Stanford, CA 94305, USA

5 Axiomatic AI, Inc., Cambridge, MA 02139, USA

* dbuterak@umd.edu, † jpzwolak@nist.gov

Abstract

Recent advances in machine learning (ML) have accelerated progress in calibrating and operating quantum dot (QD) devices. However, most ML approaches rely on access to large, representative datasets designed to capture the full spectrum of data quality encountered in practice, with both high- and low-quality data for training, benchmarking, and validation, with labels capturing key features of the device state. Collating such datasets experimentally is challenging due to limited data availability, slow measurement bandwidths, and the labor-intensive nature of labeling. QDFlow is an open-source physics simulator for multi-QD arrays that generates realistic synthetic data with ground-truth labels. QDFlow combines a self-consistent Thomas-Fermi solver, a dynamic capacitance model, and flexible noise modules to simulate charge stability diagrams and ray-based data closely resembling experiments. With an extensive set of parameters that can be varied and customizable noise models, QDFlow supports the creation of large, diverse datasets for ML development, benchmarking, and quantum device research.

Copyright attribution to authors.

This work is a submission to SciPost Physics Codebases.

License information to appear upon publication.

Publication information to appear upon publication.

Received Date

Accepted Date

Published Date

Contents

1	Introduction	2
2	Physics simulation	4
2.1	Nanowire model	4
2.2	Thomas-Fermi solver	6
2.3	Capacitance model	7
3	Data generation	9
4	Noise	11
5	Benchmarking and limitations	14

38	6 Conclusion	16
39	References	17

40
41

42 1 Introduction

43 Among the various quantum computing platforms, quantum dots (QDs) stand out for their
44 scalability potential, compact size, and long coherence times [1]. Operating QD devices, how-
45 ever, remains a formidable challenge, with complexity growing rapidly—often exponentially—
46 as the number of qubits increases. Recent advances in integrating machine learning (ML) with
47 quantum device operation have begun to mitigate these difficulties, offering promising auto-
48 mated control and calibration strategies. For example, ML algorithms have been developed for
49 the fabrication [2, 3], characterization [4, 5], tuning [6–13], and gate virtualization [14, 15]
50 of QD devices.

51 Developing robust ML models requires access to large and diverse datasets representative
52 of the multi-dimensional parameter space typical of QD devices. Crucially, for supervised ML
53 applications, these datasets must also include metadata that identifies key features, such as
54 the global state (i.e., the number of QDs formed), the charge configuration, and the type of
55 transition lines present. Unfortunately, large volumes of high-quality experimental data can be
56 challenging to obtain as companies and research groups often keep such data proprietary [16].
57 Limited measurement bandwidth in real-world experiments also constrains the efficient explo-
58 ration of the entire high-dimensional parameter space in a reasonable time. Generating ac-
59 curate feature labels for publicly available data is a labor-intensive and time-consuming task
60 that can produce subjective and potentially erroneous labels. Physics-based simulations offer
61 a practical solution: they enable the generation of arbitrarily large datasets while providing di-
62 rect access to the ground-truth charge states, thereby simplifying the labeling process needed
63 for ML training.

64 Here, we introduce QDFlow, an open-source Python package for simulating QD systems
65 and generating synthetic data tailored for ML training and applications. The core physics
66 engine in QDFlow employs the Thomas-Fermi approximation to numerically solve for the semi-
67 classical charge density $n(x)$ along a one-dimensional (1D) nanowire. While the current state-
68 of-the-art devices are typically realized by confining charges (electrons or holes) within a two-
69 dimensional (2D) heterostructure, the QDs are ultimately formed within quasi-1D channels
70 within those heterostructures, motivating our choice of a 1D model. In practice, the simulated
71 data produced by QDFlow closely resembles that of linear QD arrays in 2D heterostructures.
72 ML models trained on QDFlow-generated data have been shown to generalize effectively to
73 larger 2D QD arrays [14].

74 There are several open-source QD device simulators that rely on the constant capacitance
75 model, treating the array of QDs and their associated electrostatic gates as nodes in a network
76 of fixed capacitors [17–19]. Additionally, Ref. [19] allows the capacitances to vary with re-
77 spect to the number of charges n by introducing an n -dependent correction to the capacitance
78 matrix. In contrast, in QDFlow the capacitance parameters are physics-informed, obtained di-
79 rectly from the self-consistent Thomas-Fermi solution rather than imposed heuristically. All key
80 physical observables—such as current, charge states, and sensor readouts—are derived from a
81 capacitance model constructed based on the computed charge density $n(x)$. This ensures that
82 the capacitances evolve dynamically with gate voltages, yielding a more realistic description of
83 device behavior. Furthermore, QDFlow allows for modeling regions with low barriers between

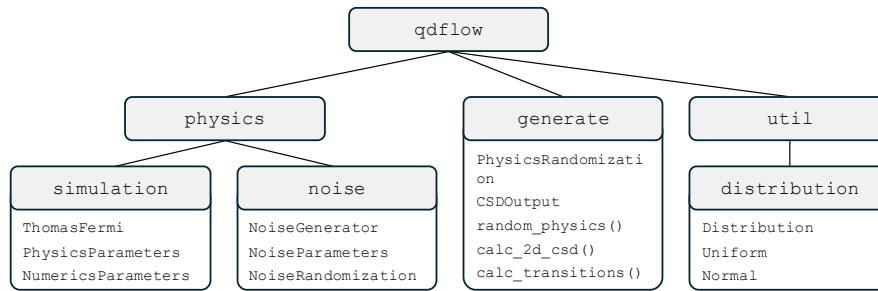


Figure 1: Diagram illustrating the QDFlow library organizational structure. Each of QDFlow’s four modules is listed, along with the most important classes or functions within those modules.

84 dots, leading the dots on either side to combine into a single centralized dot. Finally, QDFlow
 85 incorporates a flexible noise module, enabling the addition of experimentally relevant effects
 86 such as thermal broadening, charge offset drift, and voltage fluctuations. These features make
 87 the simulated data qualitatively comparable to experimental measurements while maintain-
 88 ing full access to the ground truth labels required for ML applications. Building on QFlow—a
 89 legacy implementation of the QD simulator that applied the Thomas-Fermi approximation to
 90 model charge densities and stability diagrams [20, 21]—QDFlow extends these methods into a
 91 flexible, open-source framework that integrates physics-informed capacitance modeling with
 92 realistic noise processes tailored for ML applications.

93 QDFlow has already demonstrated its utility in advancing ML-driven QD research, con-
 94 firming that ML models trained exclusively on simulated data can be successfully deployed
 95 in experimental settings, on samples fabricated in an academic cleanroom as well as on an
 96 industrial 300-mm process line, and on 1D and 2D QD arrays. The legacy version of the
 97 simulator was used to generate the QFlow-lite dataset [21, 22], which enabled the train-
 98 ing of several ML models for global state recognition. The utility of these ML models was
 99 demonstrated both offline, by navigating the voltage space within pre-measured experimen-
 100 tal datasets [13, 20], and in closed-loop experiments [9, 12, 23]. The dataset also supported
 101 the development of a novel classification framework for simple high-dimensional geometri-
 102 cal structures, known as the *ray-based classification* (RBC) framework [24]. The expanded
 103 dataset, QFlow 2.0: Quantum dot data for machine learning [22], generated using
 104 the Thomas-Fermi solver with integrated realistic noise processes, further advanced ML-based
 105 approaches to QD tuning. In particular, models trained with data from the QFlow 2.0 dataset
 106 have been successfully applied to tasks such as data quality assessment [25], physics-informed
 107 RBC and ray-based navigation in 1D QD arrays [13], and the development of a full virtu-
 108 alization stack for 1D and 2D QD arrays in Ge/SiGe [14] and in Si/SiGe. These successes
 109 confirm the compatibility of QFlow 2.0-generated with real-world experiments. They also
 110 highlight the value of physics-informed synthetic datasets for accelerating the development of
 111 automated control tools for QD systems.

112 QDFlow is available for download from the [Python Package Index](#), with the source code
 113 released under the GNU General Public License in the QDFlow GitHub repository [26]. Com-
 114 prehensive API documentation is provided via docstrings embedded in the source code and as
 115 HTML pages hosted on [Read the Docs](#). The library includes type hints for all classes and func-
 116 tions to support clarity, maintainability, and extensibility. Unit and benchmark tests are also
 117 distributed with the QDFlow repository to facilitate validation and performance evaluation.

118 2 Physics simulation

119 QDFlow has three main modules: `simulation`, `noise`, and `generate`, and one utility mod-
120 `ule`, `distribution`, as depicted in Fig. 1. The `simulation` and `noise` modules are part
121 of the `physics` package. The core physics-based engine of the simulator is contained in
122 the `simulation` module. It uses a Thomas-Fermi solver to find the stable charge configu-
123 ration and sensor output of a particular QD device defined by a set of physical parameters.
124 The QDFlow Thomas-Fermi solver was first introduced in Ref. 21, but has since been refined
125 and extended within QDFlow to improve flexibility, physical relevance, and integration with
126 downstream ML workflows. The `PhysicsParameters` dataclass, which is used to initialize
127 the simulation, specifies over twenty parameters governing the properties of the QD device.
128 These parameters include both material characteristics and device-specific features such as
129 gate geometry and positioning. Importantly, the gate voltages—experimentally relevant con-
130 trol knobs—are explicitly included among the simulation inputs. By sweeping these voltages,
131 QDFlow produces the final outputs: 2D CSDs and 1D rays, directly mirroring the tuning pro-
132 cedures used in real QD experiments.

133 The `noise` module is responsible for adding noise to the final datasets, as well as for
134 applying certain post-processing to the data. The `generate` module contains high-level func-
135 tions to assist in generating datasets. It is the module that the user would most often inter-
136 act with. Finally, the `distribution` module, contained within the `util` package, contains
137 classes defining random variable distributions.

138 To generate data with QDFlow, the user first chooses whether to run the default configu-
139 ration or adjust the distributions and ranges over which physics parameters are randomized.
140 Next, they create one or more sets of randomized device parameters, and for each device,
141 generate a CSD using the functions in the `generate` module. Once the physics parameters
142 have been specified, an instance of the `ThomasFermi` class is instantiated. This class serves
143 two main purposes: first, it solves for the charge density function $n(x)$; and second, it uses
144 $n(x)$ to construct a capacitance model and compute physical quantities such as the device’s
145 charge state and sensor response. QDFlow then runs the physics simulation for every pixel in
146 each diagram and compiles the results into a `CSDOutput` dataclass, which is returned to the
147 user. By repeating this process over a range of gate voltages, QDFlow generates data that can
148 be assembled into CSDs or rays, depending on the application. The output, stored as NumPy
149 arrays, can be directly analyzed and plotted, or optionally augmented with noise to emulate
150 experimental data.

151 In the following sections, we provide a more detailed account of the nanowire model
152 physics underlying the simulation. We then explain how the Thomas-Fermi approximation
153 is applied to construct the capacitance model that drives the CSD simulation.

154 2.1 Nanowire model

155 QDFlow employs a 1D physics model in which charges are assumed to be confined to a linear
156 nanowire that lies along the x -axis. The ends of the nanowire are connected to electron reser-
157 voirs, and a bias voltage can be applied between them. Electrostatic gates are positioned at a
158 height h below the xy -plane, and are modeled as infinite cylindrical conductors with central
159 axis parallel to the y -axis, as shown in Fig. 2(a). The arrangement makes our nanowire model
160 a hybrid between a true nanowire device and other QD device architectures. Gates biased to
161 low potential act as plunger gates, while those biased to high potential act as barrier gates (for
162 positive charge carriers, with the convention reversed for negative carriers).

163 The plunger and barrier gates define an electrostatic potential $V(x)$, where x is the distance
164 along the nanowire. Note that because we are using a 1D model, we are only concerned
165 with the potential along the x -axis. The potential at a distance r from the center of a single

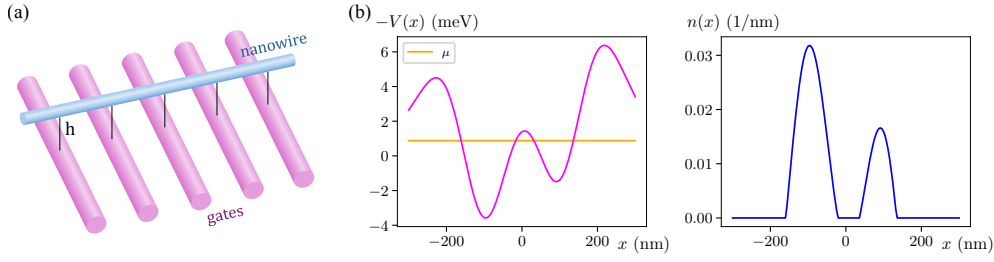


Figure 2: **(a)** The nanowire model used in QDFlow. **(b)** The potential $V(x)$ created by the electrostatic gates (left) and the charge density $n(x)$ induced by the potential (right).

166 cylindrical gate (in the absence of other gates) can be expressed as the potential of a screened
 167 line charge:

$$V_{\text{gate}}(r) = V_h \frac{\mathcal{K}_0(r/\lambda)}{\mathcal{K}_0(h/\lambda)} \quad (1)$$

168 where V_h is the potential at a reference distance $r = h$ (chosen as the separation between the
 169 gate and the nanowire), λ is the screening length, and $\mathcal{K}_0(z)$ is the modified Bessel function
 170 of the second kind. Specifically, we note that V_h is not the voltage of the gate itself; rather, it
 171 is the voltage that the nanowire feels due to the gate (in the absence of other gates). This is
 172 essentially the voltage of the gate multiplied by the lever arm of the gate.

173 Because the presence of nearby gates induces additional charges on each of the gates,
 174 and consequently changes Eq. (1), we cannot obtain $V(x)$ by simply summing $V_{\text{gate}}(r)$ over
 175 all gates. Determining the exact potential in the presence of multiple gates is a challenging
 176 electrostatics problem, even in the purely classical setting. It requires solving the screened
 177 Laplace equation with boundary conditions determined by the voltages on each of the gates.
 178 While such a calculation can be performed numerically, it must be repeated whenever any gate
 179 voltage is changed.

180 To make the problem tractable, we adopt the simplifying assumption that the induced
 181 charges on each gate are rotationally symmetric about the axis of the gate. Under this ap-
 182 proximation, the induced charges act as a line charge that lies along the central axis of the
 183 gate. Because the gate is rotationally symmetric, the potential $V_{\text{gate}}(r)$ also acts as a single line
 184 charge at the center of the gate, and thus the induced charges effectively rescale $V_{\text{gate}}(r)$ by a
 185 constant factor. Let V'_i be the rescaled value of V_h for gate i after including the effects of the
 186 induced charges on gate i , and let V_i be the value of V_h necessary for $V_{\text{gate}}(r)$ to give the actual
 187 potential of gate i . Then by the superposition principle, V_i can be determined by adding the
 188 potential contributions from each of the gates:

$$V_i = \sum_j A_{ij} V'_j \quad (2)$$

189 where A_{ij} denotes the ratio between the contribution from gate j to the potential at gate i
 190 and the effective potential V'_j . In the absence of other gates, $V_i = V'_i$, so A_{ii} is simply 1. The
 191 contribution from one gate to another is given by $V_{\text{gate}}(r)$, where r is the distance between
 192 gates. Thus, A_{ij} can be expressed as follows:

$$A_{ij} = \begin{cases} 1 & \text{if } i = j \\ V_{\text{gate}}(x_j - x_i) / V_{\text{gate}}(\rho_j) & \text{otherwise,} \end{cases} \quad (3)$$

193 where x_j is the x-coordinate of the central axis of gate j and ρ_j is the radius of the gate j .
 194 Calculating and inverting the matrix \mathbf{A} allows us to determine the effective potentials V'_i from
 195 the applied gate voltages V_i . We then obtain $V(x)$ by summing $V_{\text{gate}}(\sqrt{(x-x_i)^2 + h^2})$ over
 196 all gates and using the effective potentials V'_i in place of V_h in Eq. (1).

197 2.2 Thomas-Fermi solver

198 Having established how to compute the effective gate potentials and construct $V(x)$, we now
 199 turn to the resulting charge distribution along the nanowire. Define $n(x)$ to be the linear
 200 charge density at a point x along the nanowire, which is determined in response to the po-
 201 tential $V(x)$, as illustrated in Fig. 2(b). However, due to the Coulomb interaction between
 202 charges, the presence of an induced charge in the nanowire will create a correction to $V(x)$.
 203 This self-interaction results in the following integral equations, which must be solved self-
 204 consistently:

$$n(x) = \int_{\epsilon'(x)}^{\infty} \frac{g_0}{1 + e^{\beta(\epsilon - \mu)}} d\epsilon = \frac{g_0}{\beta} \text{sp}[\beta(\mu - \epsilon'(x))] \quad (4)$$

$$\epsilon'(x) = qV(x) + \int_{\mathbb{R}} K(x, x') n(x') dx' \quad (5)$$

205 The physical parameters μ , g_0 , and β in Eq. (4) indicate the Fermi level, the density of states
 206 in the conduction band (which is constant in 2D), and the inverse temperature, respectively,
 207 and $\text{sp}(z) = \ln(1 + e^z)$ is the softplus function. Parameter q in Eq. (5) controls the sign of the
 208 charge carriers, with -1 indicating electrons and $+1$ indicating holes, while $K(x, x')$ gives the
 209 strength of the Coulomb interaction between points x and x' , and is defined as follows:

$$K(x, x') = \frac{K_0}{\sqrt{(x - x')^2 + \sigma^2}} \quad (6)$$

210 where K_0 defines the energy scale of the interaction and σ is a softening parameter added to
 211 prevent a numerical singularity at $x = x'$, which occurs due to the 1D model breaking down at
 212 scales less than the radius of the nanowire. The value of σ can be chosen to be $3\pi r/8$, where
 213 r is the nanowire radius, to maintain consistency with the potential energy of two uniformly
 214 charged disks as the spacing between them approaches zero [27], or alternatively, a custom
 215 interaction $K(x, x')$ can be provided.

216 The Coulomb integral in Eq. (5) is formally taken over the entire nanowire. Because
 217 $K(x, x')$ scales for large x' as $1/|x'|$, this introduces concerns that the integral might diverge.
 218 At the same time, the integrand is weighted by $n(x')$, which becomes exponentially small for
 219 $V(x') - \mu \gg \beta^{-1}$. This condition is satisfied at the external barriers, see Fig. 2(b), provided that
 220 the external barrier voltages are sufficiently high. In addition, it is assumed that at distances
 221 far away from the nanowire, the system is connected to an electron reservoir where $n(x')$ is
 222 large. However, the Coulomb interaction in semiconductors tends to include a screening term
 223 that suppresses contributions past a certain range. Thus, in practice, it is sufficient to evaluate
 224 the integral between the two external barrier gates.

225 For convenience, we define a linear operator \mathbf{K} to be the result of evaluating the Coulomb
 226 integral as follows:

$$\mathbf{K}f(x) = \int_{\mathbb{R}} K(x, x') f(x') dx' \quad (7)$$

227 This allows us to combine Eqs. (4) and (5) to obtain:

$$n(x) = \frac{g_0}{\beta} \text{sp}[\beta(\mu - qV(x) - \mathbf{K}n(x))]. \quad (8)$$

228 The basic method we employ to solve Eq. (8) is successive iteration. Starting from an initial
 229 guess $n_0(x)$, the right-hand side of Eq. (8) is evaluated with $n(x) = n_0(x)$, yielding an updated
 230 function $n_1(x)$. This procedure is then repeated until $n(x)$ converges, if at all. The con-
 231 vergence tolerance and the maximum number of allowed iterations are specified through the

232 `NumericsParameters` dataclass, which can be provided when instantiating the `ThomasFermi`
 233 class. If the iteration does not converge to the specified tolerance within the allowed number
 234 of iterations, a `ConvergenceWarning` is issued.

235 The convergence can be problematic for certain parameter regimes. For example, if we
 236 define $\Delta(x)$ to be the difference between an initial guess $n_0(x)$ and the true value $n(x)$:

$$n_0(x) = n(x) + \Delta(x), \quad (9)$$

237 then evaluating the right-hand side of Eq. (8) yields:

$$n_1(x) = \frac{g_0}{\beta} \text{sp}[\beta(\mu - qV(x) - \mathbf{K}n(x) - \mathbf{K}\Delta(x))] \quad (10)$$

238 We now use the approximation $\text{sp}(z) \approx z$, which is valid for $z \gg 1$. Although this assumption
 239 does not always hold (particularly for small β), it is useful for analyzing certain convergence
 240 issues that may arise. Under this approximation, Eq. (10) simplifies to:

$$n_1(x) \approx n(x) - g_0\mathbf{K}\Delta(x) \quad (11)$$

241 If all eigenvalues of $g_0\mathbf{K}$ are smaller than 1, the error term $-g_0\mathbf{K}\Delta(x)$ will be smaller in
 242 magnitude than the initial error $\Delta(x)$, and successive iterations will therefore converge to
 243 $n(x)$. Conversely, if $g_0\mathbf{K}$ possesses eigenvalues greater than 1, the iterative scheme will gen-
 244 erally diverge. Physically, this divergence corresponds to strong coupling between charges, a
 245 regime that is well known to cause convergence difficulties in condensed matter systems [28].
 246 Fortunately, this issue can be partially mitigated by solving Eq. (9) for $\Delta(x)$, substituting the
 247 result into Eq. (11), and solving for $n(x)$, yielding the following expression:

$$n(x) \approx (\mathbf{1} + g_0\mathbf{K})^{-1} [g_0\mathbf{K}n_0(x) + n_1(x)] \quad (12)$$

248 If we discretize the x -axis, the operator $(\mathbf{1} + g_0\mathbf{K})^{-1}$ can be computed through direct matrix
 249 inversion. This expression can then be incorporated into the successive iteration scheme by
 250 applying Eq. (12) after each iteration. Although there are still parameter regimes where the
 251 process diverges, this modified approach drastically enlarges the domain of convergence. In
 252 the weak-interaction limit, where the eigenvalues of $g_0\mathbf{K} \ll 1$, the right-hand side of Eq. (12)
 253 simplifies to $n_1(x)$ to leading order in $g_0\mathbf{K}$. Thus, in this limit, the method naturally recovers
 254 the standard successive iteration procedure.

255 2.3 Capacitance model

256 After calculating $n(x)$, `QDFlow` employs a capacitance model to determine the stable charge
 257 configuration and other properties. Similar techniques have been implemented in other QD
 258 simulations [17–19]. In most of those approaches, the capacitance matrix is assumed to be
 259 constant, i.e., the interdot capacitances remain fixed as the gate voltages are swept. The sim-
 260 ulation introduced in Ref. 19 allows for variable capacitances by applying a correction to the
 261 capacitance matrix based on the particle number. In contrast, `QDFlow` derives the capacitance
 262 matrix directly from the charge density $n(x)$, which depends explicitly on the gate voltages.
 263 This feature enables charge-transition slopes and spacings to vary across a single CSD. More-
 264 over, constructing the capacitance model from $n(x)$ naturally captures transitions between a
 265 double dot and a merged single dot as the interdot barrier is lowered.

266 The first step in creating the capacitance model is determining the regions of the nanowire
 267 where significant amounts of charge are induced. This is achieved by applying a threshold to
 268 $n(x)$, configurable through the `NumericsParameters` dataclass, and identifying continuous
 269 intervals of points that lie above the threshold. This will result in a set of intervals of the form

270 $[a_i, b_i]$, which we call “charge islands.” The thresholding is also responsible for determining
 271 whether or not adjacent QDs should be handled as individual dots. Specifically, if $n(x)$ exceeds
 272 the threshold throughout the region between the two QDs, they are merged and treated as a
 273 single dot. Otherwise, they are considered to be two separate QDs with a potential barrier
 274 between them.

275 Once the charge islands are identified, the energy E of the resulting capacitance model is
 276 defined as follows:

$$E = \sum_{i,j} E_{ij}(Q_i - Z_i)(Q_j - Z_j) \quad (13)$$

$$Z_i = \int_{a_i}^{b_i} n(x) dx \quad (14)$$

$$E_{ij} = \frac{1}{Z_i Z_j} \left[c_k \delta_{ij} \int_{a_i}^{b_i} n(x)^2 dx + \frac{1}{2} \int_{a_i}^{b_i} \int_{a_j}^{b_j} K(x, x') n(x) n(x') dx dx' \right] \quad (15)$$

277 where Z_i is the (potentially noninteger) charge induced by the gates on island i under the
 278 Thomas-Fermi approximation, and Q_i is the integer number of charges on island i under a
 279 specific charge configuration \vec{Q} . The c_k term of Eq. (15) incorporates the kinetic energy of
 280 the charges. Since, for our purposes, the energy matrix fully characterizes the system, we do
 281 not compute the capacitances explicitly and instead work directly with the energy matrix. If
 282 desired, the capacitance matrix \mathbf{C} can be obtained from the energy matrix via the relationship
 283 $\mathbf{C} = (2\mathbf{E})^{-1}$.

284 After calculating the energy matrix, the next step is to determine the charge configuration
 285 \vec{Q} that minimizes the total energy E , subject to the constraint that all Q_i must be nonneg-
 286 ative integers. This is an instance of an integer optimization problem, which in general is
 287 NP-complete. However, for a moderate number of gates, a brute-force search is sufficient to
 288 find the minimum. In particular, we first locate the minimum in the continuous space, which
 289 occurs at \vec{Z} , and then evaluate $E(\vec{Q})$ over all \vec{Q} such that for each integer Q_i , $|Q_i - Z_i| < 1$.
 290 Once a stable charge configuration is identified, the potential at each of the sensors is calcu-
 291 lated under the assumption that each island i hosts a line of charge with total charge $q Q_i$ and
 292 charge density proportional to $n(x)$. The Coulomb potential at each of the sensors arising from
 293 these charge islands is calculated, and the result is normalized by dividing by the potential of
 294 a single point charge located at a point on the nanowire closest to the sensor in question. This
 295 means that a single transition should have a height of no more than 1 after normalization.

296 Finally, QDFlow allows the current across the nanowire to be found. For this calculation,
 297 the left and right sides of the nanowire are assumed to be connected to electron baths with po-
 298 tentials V_L and V_R , respectively. The dynamics of the charges are modeled using a semi-classical
 299 approach, treating them as particles that travel at the Fermi velocity. Each time they collide
 300 with a barrier, the particles have a chance to either tunnel through it or be reflected back. The
 301 tunneling probability across each barrier is determined by the transmission coefficient, which
 302 we calculate using the WKB approximation. This allows the tunneling rates between islands
 303 and the tunneling rates to and from the external charge baths to be obtained. These tunnel
 304 rates are then used to define a Markov graph which encodes the dynamics of the transitions
 305 between charge states. The current through the nanowire is obtained by evaluating the net
 306 rate at which charges enter and leave the charge baths at the steady state of this Markov graph.

307 3 Data generation

308 The data generation is carried out within the `generate` module. A single instance of the
309 `ThomasFermi` class calculates quantities of interest for a single point in voltage-space only
310 based on the device configuration specified in the `physics` module. To generate a complete
311 CSD, a new simulation instance must be created for each pixel. However, since the gate volt-
312 ages of neighboring pixels vary only slightly, it follows that the corresponding charge density
313 $n(x)$ will also not change significantly between adjacent pixels. To optimize QDFlow perfor-
314 mance, the result of the $n(x)$ calculation at one pixel is used as an initial condition when
315 calculating $n(x)$ at adjacent pixels. This means that $n(x)$ must only be calculated from scratch
316 once for each diagram.

317 QDFlow contains convenience functions for generating CSDs and rays in the `generate`
318 module. Since the primary purpose of QDFlow is to generate data for training specialized ML
319 models, it is essential that the resulting dataset captures the full range of variability observed
320 in contemporary QD devices. To achieve this, QDFlow includes functionality to randomize
321 nearly all physics parameters and to control the distributions from which each parameter is
322 drawn. This capability is implemented via the `PhysicsRandomization` dataclass, which
323 specifies each physics parameter as either a fixed value (when no randomization is desired,
324 e.g., to allow regeneration of the same QD device), or a `Distribution` from which to draw
325 the random values. A code example in Listing 1 shows how to import QDFlow and how to
326 initialize a random configuration of physical parameters, with μ drawn from a distribution
327 provided by the user.

328 The `Distribution`, defined in the `distribution` module, is an abstract base class that
329 encodes how a given parameter should be randomized. Several standard distributions, in-
330 cluding `Uniform`, `Normal`, and `LogNormal`, are implemented in QDFlow as wrappers to the
331 NumPy random generator functions of the same name. In addition, user-defined distributions
332 can be easily created by extending the `Distribution` class and implementing the `draw()`
333 method to generate random values in an arbitrary manner. The `CorrelatedDistribution`
334 class handles cases where it is desired or necessary for multiple random variables to be related
335 to one another in some way.

336 This randomization framework, along with the dozens of configurable physics parame-

```
1 from qdflow import generate
2 from qdflow.util import distribution
3
4 # Create a new dataclass instance that contains the default
5 # randomization distributions for each physics parameter
6 phys_rand = generate.PhysicsRandomization.default()
7
8 # Change the range from which mu can be drawn
9 phys_rand.mu = distribution.Uniform(0, 1.2)
10
11 # Generate a list of 6 sets of random device parameters
12 n_devices = 6
13 phys_params = generate.random_physics(phys_rand, n_devices)
```

Listing 1: Example code to generate a list of 6 randomized sets of device parameters. First, a `PhysicsRandomization` object is created, which defines the ranges and distributions, as appropriate, from which the physics parameters should be randomized. Distributions for each parameter can then be set as desired.

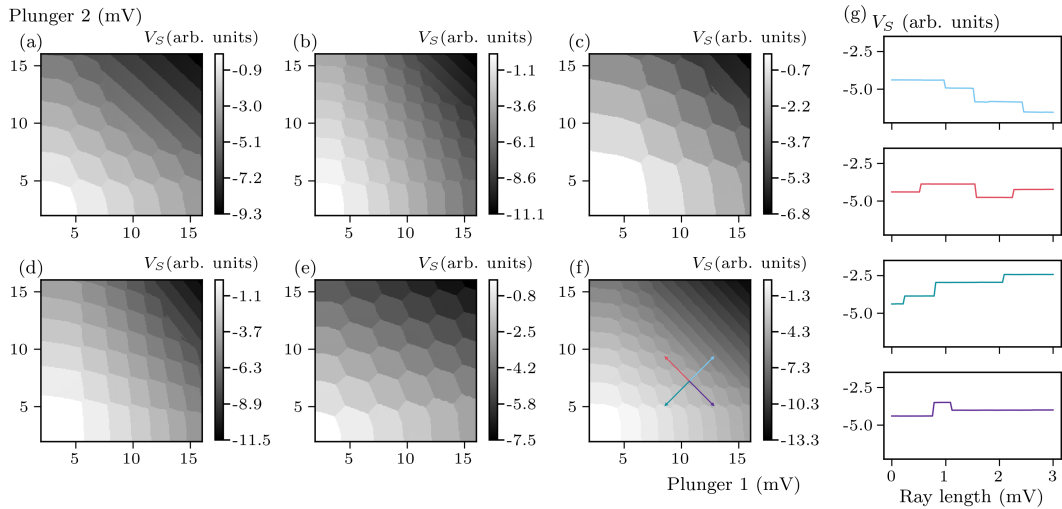


Figure 3: (a)-(f) Examples of CSDs generated with randomized physics parameters. (g) Examples of ray data generated along the rays shown on the CSD in panel (f).

337 ters, enables QDFlow to generate a highly diverse set of CSDs. Figure 3 shows six examples
 338 of CSDs generated with QDFlow. A snippet of code allowing to generate CSD data from a
 339 `PhysicsParameters` object is shown in Listing 2.

340 While CSDs are extremely useful for visualizing charge states, they require extensive data
 341 collection. In practice, only a relatively small subset of points—the charge transitions—are
 342 of primary importance. As the number of dots grows, so does the dimensionality of the gate
 343 voltage space, rapidly making the exploration of the complete, multidimensional voltage space
 344 infeasible. This challenge is typically handled by measuring multiple 2D CSDs, each defined
 345 by a different pair of gates.

346 In Ref. 12, an alternative method for assessing the charge state in QD devices, with 1D rays
 347 measured in multiple directions in the voltage space used in place of the 2D CSDs. This method
 348 greatly reduces the amount of data required for assessing the charge state of the device, but

```

1  from qdflow import generate
2  import numpy as np
3
4  # Create a set of physics parameters
5  phys = generate.default_physics(n_dots=2)
6
7  # Set ranges (in mV) and resolution of plunger gate sweeps
8  V_x = np.linspace(2., 16., 100)
9  V_y = np.linspace(2., 16., 100)
10
11 # Generate a charge stability diagram
12 csd = generate.calc_2d_csd(phys, V_x, V_y)
13
14 # Obtain the sensor readout in the form of a numpy array
15 sensor_num = 0
16 sensor_readout = csd.sensor[:, :, sensor_num]
```

Listing 2: Example code demonstrating how to generate a CSD from a `PhysicsParameters` object.

```

1  from qdflow import generate
2  import numpy as np
3  from scipy.stats import qmc
4
5  # Create a set of physics parameters
6  phys = generate.default_physics(n_dots=2)
7
8  # Generate quasirandom points inside a given area
9  v_min, v_max = 2., 16.
10 point_generator = qmc.Halton(d=2, scramble=False)
11 initial_points = qmc.scale(point_generator.random(n=50), v_min, v_max)
12
13 # Define a list of rays that will extend out from each point
14 ray_length = 3. # length of rays in mV
15 num_rays = 8
16 rays = ray_length * np.array([[np.cos(2*np.pi*i/num_rays),
17                               np.sin(2*np.pi*i/num_rays)] for i in range(num_rays)])
18
19 # Generate ray data
20 resolution = 100 # points per ray
21 ray_data = generate.calc_rays(phys, initial_points, rays, resolution)

```

Listing 3: Example code demonstrating how to generate ray data from a `PhysicsParameters` object.

349 sacrifices some of the intuitive human interpretability provided by CSDs, necessitating the
350 use of ML tools. To support the development of ML methods for ray-based analysis, QDFlow
351 includes functionality for generating ray-based datasets, as shown in Listing 3.

352 4 Noise

353 The simulations described thus far capture many essential physical features of QD devices but
354 omit one critical ingredient: noise. In experimental data, noise strongly influences both the
355 visibility of charge transitions and the reliability of automated analysis.

356 To more faithfully emulate experimental conditions, QDFlow includes the noise module,
357 which contains functionality for adding noise to both CSDs and rays, as well as several postpro-
358 cessing functions designed to mimic effects of experimental measurements. The module imple-
359 ments several types of noise, including the white noise, pink ($1/f$) noise, telegraph noise, and
360 latching effects, as well as stray transitions arising from nearby unintended dots [25,29]. Post-
361 processing functions include adding gate-sensor coupling, adding a $\text{sech}^2 x$ blur, and adding
362 Coulomb peak effects. Each noise in QDFlow can be controlled individually, with its magnitude
363 defined relative to the scale of the CSD data, or as a predefined mixture. Similar to the physical
364 parameter randomization discussed in Sec. 3, QDFlow supports designating the distributions
365 from which each noise parameter is drawn via the `NoiseRandomization` dataclass.

366 Figure 4(a) shows an example of a noiseless CSD simulated with QDFlow. CSDs with
367 noise implementations adapted from QFlow—white, pink, and telegraph noise and Coulomb
368 peak—are depicted in panels (b), (c), (d), and (e), respectively. CSDs with latching, sech^2
369 blur, unintended QD, and sensor-gate coupling—new to QDFlow—are presented in panels (f),
370 (g), (h), and (i), respectively.

371 The simplest, white noise, is implemented by adding to each pixel a value drawn from a

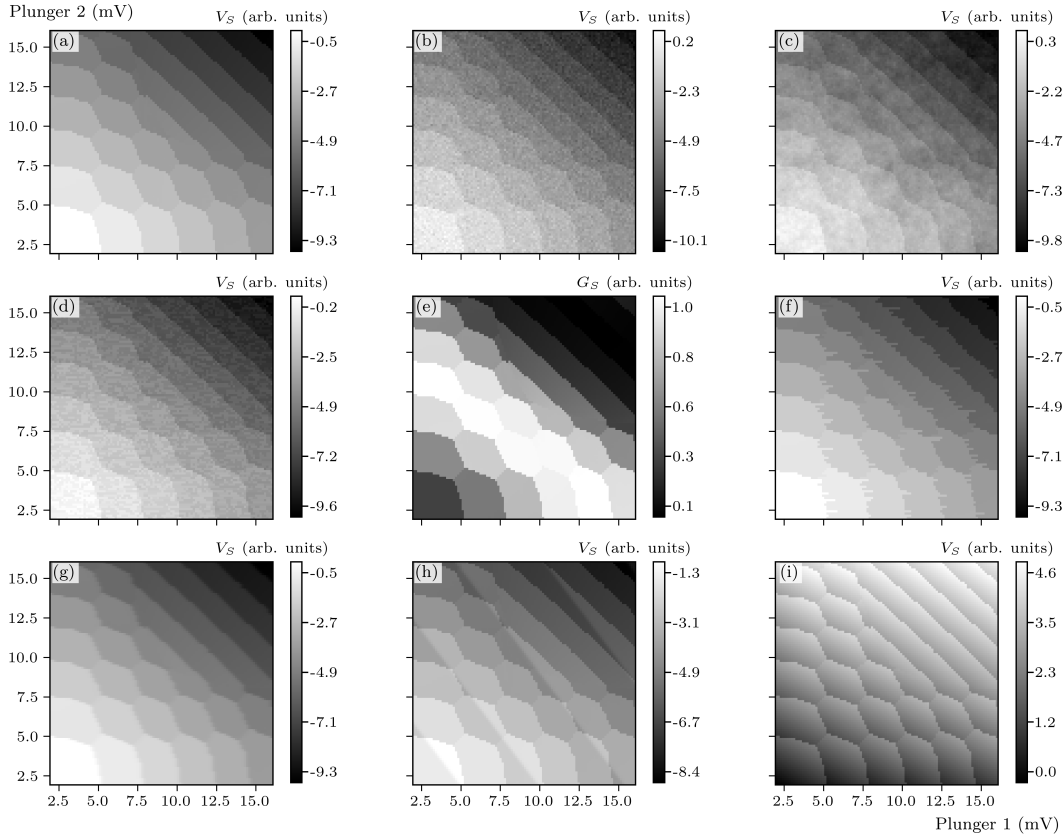


Figure 4: Examples of noise added to a CSD. (a) The original CSD data, (b) white noise, (c) pink noise, (d) telegraph noise, (e) Coulomb peak, (f) latching, (g) Sech blur, (h) unintended QD, and (i) sensor-gate coupling.

372 normal distribution with standard deviation given by the magnitude of the white noise. Pink
 373 noise is implemented by generating white noise in Fourier space with a uniform random phase
 374 and magnitude proportional to $1/\sqrt{f_x^2 + f_y^2}$, where f_x and f_y are the components of each point
 375 in Fourier space, and then applying an inverse Fourier transform. This configuration allows for
 376 greater variability compared to telegraph noise. Alternatively, QDFlow also provides the option
 377 to add pink noise correlated along only the primary measurement axis, which corresponds to
 378 the more physical model of pink noise correlated in time.

379 Telegraph noise is applied along an axis corresponding to the primary measurement direc-
 380 tion in experimental data. It consists of adding a value (drawn from a normal distribution with
 381 nonzero mean) to a line of several contiguous pixels. The length of the added line is randomly
 382 drawn from a geometric distribution. This allows the distribution of lengths of the telegraph
 383 noise to follow an exponential, as expected for two-level systems with finite excited-state life-
 384 times. This process is then repeated across the CSD, alternating the sign of the value added
 385 each time.

386 Transitions from spurious QDs are emulated by adding functions of the form $\tanh((\vec{x}-\vec{x}_0)\cdot\vec{a})$,
 387 where \vec{x} gives the coordinates of each pixel, \vec{x}_0 is the location on the CSD of the transition,
 388 and \vec{a} determines how strongly each of the gates plotted on the x - and y -axes are coupled
 389 to the unintended dot. Values of \vec{x}_0 and \vec{a} are randomized, but a single \vec{a} is used if multiple
 390 unintended transitions appear on a single diagram.

391 The latching noise implemented in QDFlow can be controlled using one of two methods.
 392 The first and simpler legacy method to simulate latching is to shift each row of pixels by a ran-

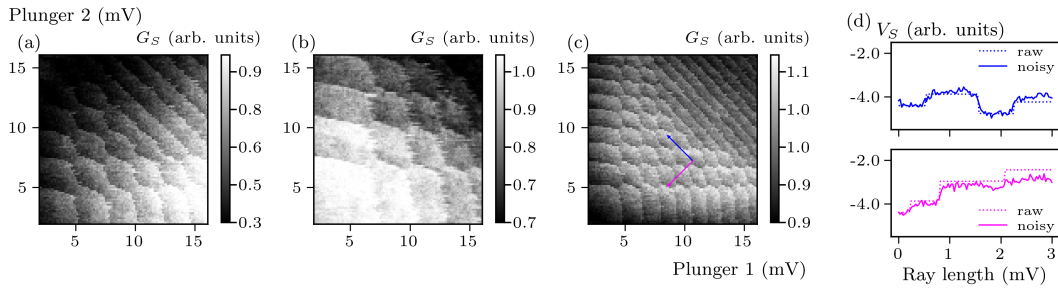


Figure 5: (a)-(c) Examples of CSDs with all noise types combined. (d) Ray data without noise (dotted line) and with noise added (solid line).

dom number of pixels drawn from a geometric distribution. This process produces a latching-like effect along the charge transitions; however, it is somewhat unrealistic since all transitions on the same row are shifted by the same amount, and because pixels far away from transitions are also displaced. A more physically realistic method relies on the nanowire simulation to calculate the sensor readout for both an excited charge state and a stable state at each pixel, similar to what is implemented in Ref. 18. The excited state chosen corresponds to the charge configuration most recently occupied prior to the most recent transition when sweeping the gate voltages. When latching noise is added, the sensor readout from the excited state replaces the stable-state readout for the first few pixels after each transition, with the number of pixels randomized each instance. In general, the second method is preferable as it more accurately reflects the experimental conditions; however, the first, legacy method is provided as a fallback when excited-state data are unavailable or computationally inconvenient, or impossible to obtain.

In addition to noise, several postprocessing functions can be applied to the data. A sensor-gate coupling in the form of a linear gradient along a random direction can be added. Convolution with a $\text{sech}^2 x$ kernel along the measurement axis introduces smoothing of the sharp transitions.

Finally, it is important to note that the physics simulation returns the value of the potential at each of the sensors; however, experimentally, the conductance of the sensor is the quantity that is measured. Therefore, we convert from potential to conductance by using a Coulomb peak lineshape of the form $G \propto \text{sech}^2[A(V - V_0)]$, where G is the conductance of the sensor, A is a parameter that determines the width of the Coulomb peak, V is the potential at the sensor (the simulation output), and V_0 is the peak center [30].

CSDs with a mixture of noises optimized for compatibility with experimental data are presented in Fig. 5(a)-(c). Figure 5(d) shows two rays with added noise. The exact amounts of each type of noise are randomized for each diagram. A code example showing how to generate noisy CSD data for a previously simulated sample CSD is shown in Listing 4.

Given the computational complexity of Thomas-Fermi calculations, the noise module is configured to assume that a complete noiseless CSD (or a ray-based data) has already been generated using the `generate` module. This approach gives us several advantages. First, it significantly reduces the computational overhead since multiple noise realizations with different relative noise strengths can be generated from a single noiseless CSD. Secondly, the modular approach adopted in QDFlow provides flexibility that cannot be achieved experimentally, where it is not possible to calibrate individual noise sources to the desired level. Additionally, it allows us to specify the magnitudes of each of the noise types relative to the local scale of the surrounding data points, which is important since the scale of the data points can vary across large CSDs. Finally, it allows for systematic benchmarking of ML algorithms since the noise level and type can be modified independently of the underlying physical configuration.

```

1  from qdflow.physics import noise
2  from qdflow.util import distribution
3  import numpy as np
4
5  # Use data from previous example
6  data = np.load("sensor_readout.npy")
7
8  # Create a new dataclass instance that contains the default
9  # randomization distributions for each noise type
10 noise_rand = noise.NoiseRandomization.default()
11
12 # How much noise to add, relative to the transition height upper bound
13 noise_amount = 0.15
14
15 # Use a CorrelatedDistribution to randomize the white, pink, and
16 # telegraph noise in such a way that the total always equals noise_amount
17 num_dists = 3
18 dists = distribution.SphericallyCorrelated(num_dists,
19                                             noise_amount).dependent_distributions()
20 noise_rand.white_noise_magnitude = dists[0].abs()
21 noise_rand.pink_noise_magnitude = dists[1].abs()
22 noise_rand.telegraph_magnitude = dists[2].abs()
23
24 # Generate a random set of noise parameters
25 noise_params = noise.random_noise_params(noise_rand)
26
27 # Add noise to the data
28 noisy_data = noise.NoiseGenerator(noise_params).calc_noisy_map(data)

```

Listing 4: Example code to add noise to a charge stability diagram. First, a `NoiseRandomization` object is created, which defines the ranges and distributions, as appropriate, from which the noise parameters should be randomized. A `CorrelatedDistribution` is used to randomize the different noise types while ensuring that the total noise amount is constant.

431 For example, one can generate a single noiseless dataset and then apply different realizations
432 of noise to study the robustness of a given algorithm under varying experimental conditions,
433 as was done in Ref. 13.

434 5 Benchmarking and limitations

435 To benchmark QDFlow, we find the mean runtime of the physics simulation for 10,000 ran-
436 domly generated sets of physics parameters. Each simulation is run with at most 1,000 it-
437 erations and a relative convergence tolerance of 10^{-3} . We are interested in comparing the
438 contribution to the overall runtime from calculating $n(x)$ with the remaining portion of the
439 simulation as the number of QDs increases. For each number of dots N , we obtain two run-
440 times: (i) the time required to compute the charge density profile $n(x)$, and (ii) the remaining
441 time to construct the capacitance model, minimize Eq. (13), and evaluate the sensor output.
442 The results for small- and mid-sized QD arrays are shown in Fig. 6(a) and Fig. 6(b), respec-
443 tively.

444 For a small number of dots ($N \leq 20$), the main bottleneck is the initial part of the simulation

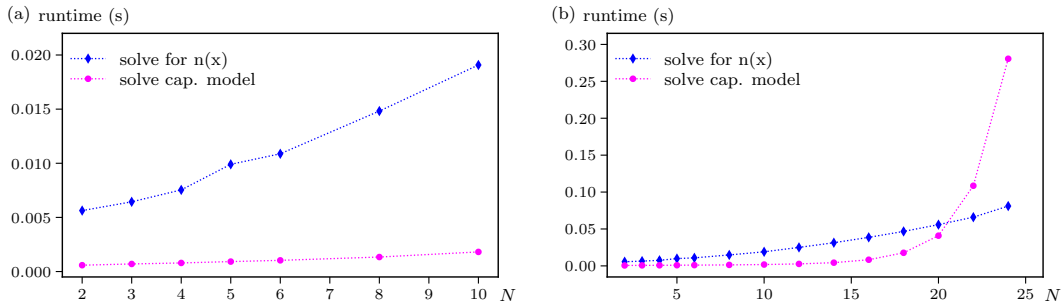


Figure 6: Average runtime versus number of dots N for (a) Thomas-Fermi solver and (b) capacitance model solver. Benchmarks were performed on a 2.8 GHz AMD Ryzen 5 7520U processor.

445 where $n(x)$ is calculated. However, as the number of dots N is increased, the minimization of
 446 Eq. (13) over integer charge configurations $\vec{Q} \in \mathbb{Z}^N$ for which the runtime scales exponentially
 447 in N begins to dominate. In practice, we expect most use cases to involve no more than ten
 448 QDs, as long-range interactions tend to be negligible due to screening from the material and
 449 the nearby gates; thus, we focus attention on the cost of computing $n(x)$ in this regime.

450 Because QDFlow calculates the capacitance model at each point in the CSD by explicitly
 451 solving for $n(x)$, it requires several orders of magnitude more runtime to generate CSDs than
 452 simulations based on constant capacitance models. Thus, for applications that require real-
 453 time data, faster simulations such as QDsim [17] or QArray [18] may be more suitable. On
 454 the other hand, for applications such as generating datasets for training and validation of ML
 455 models for autonomous control of QD systems, the higher-fidelity data provided by QDFlow—
 456 including effects such as QDs merging across low barriers—often justifies the additional com-
 457 putational cost.

458 In addition to its relatively long runtime, QDFlow has several modeling limitations. While
 459 QDFlow is based on an underlying physical nanowire model, it is designed only to produce
 460 qualitatively realistic behavior. For example, gates are modeled as infinite cylinders arranged
 461 in a simple, idealized geometry, whereas in real devices the shapes and arrangements of gates
 462 can be considerably more complex. Furthermore, the electron density $n(x)$ is calculated only
 463 in 1D, an approximation that can introduce errors for systems with non-negligible transverse
 464 extent. Finally, the simulation uses a semiclassical approach and therefore does not include
 465 correlation effects captured by, for example, the Hubbard model. Taken together, these ap-
 466 proximations prevent QDFlow from generating quantitatively accurate data.

467 QDFlow also lacks certain capabilities present in other simulators. For example, it cannot
 468 currently model closed systems with a fixed number of charges isolated from the source and
 469 drain contacts—a functionality available in QArray [18]. Finally, QDFlow is configured to
 470 model the state that minimizes the energy of the capacitance model, implicitly assuming that
 471 the system can transition freely between charge configurations. However, this assumption can
 472 break down for large arrays of QDs. For example, if a charge must transition between non-
 473 neighboring QDs passing through an intermediate QD that forms a large barrier, it may get
 474 “stuck” on one side even if it is energetically favorable to move to the other side. This will
 475 result in much more extreme latching effects than QDFlow can model.

476 QDFlow has been tested both modularly and holistically, through extensive unit testing and
 477 by comparing its output to experimental data. The QDFlow repository includes unit tests for
 478 every function in the package, ensuring coverage of all lines of code. The validity of QDFlow
 479 has been confirmed by performance of multiple specialized ML models trained on QDFlow-
 480 generated data and deployed in real-world applications, as we discuss in Sec. 1 and in Sec. 6.

481 6 Conclusion

482 Progress toward scalable quantum information technologies based on QD systems depends
483 critically on overcoming the complexity of device operation and calibration with increasing
484 number of QDs. Novel ML-based methods have emerged as powerful tools to address these
485 challenges, but their effectiveness relies on access to large, diverse, and accurately labeled
486 datasets. QDFlow was developed precisely to meet this need.

487 QDFlow differs from existing QD simulations in that it fully simulates the charge density
488 function $n(x)$. By integrating a self-consistent Thomas-Fermi solver with a dynamic capac-
489 itance model, QDFlow provides a physics-informed simulation framework that goes beyond
490 constant-capacitance approximations. This enables the generation of CSDs and ray-based data
491 with features that evolve naturally with gate voltages, mimicking experimental behavior such
492 as dot merging and transition slope variation.

493 The modular data generation tools allow for extensive randomization over physical param-
494 eters, yielding highly diverse synthetic datasets suitable for ML applications, while the noise
495 module introduces experimentally relevant effects—including thermal broadening, telegraph
496 noise, latching, and unintended transitions—in a controllable fashion. Together, these fea-
497 tures make QDFlow uniquely positioned to support both the development and benchmarking
498 of ML algorithms implemented in a wide range of tuning procedures, device architectures,
499 and material platforms. Early use cases, such as the QFlow-lite and QFlow 2.0 datasets,
500 have already demonstrated QDFlow’s ability to accelerate the training of ML models for global
501 state recognition [9, 20], ray-based navigation and charge tuning [12, 13], data quality assess-
502 ment [25], detection of spurious QDs [31], and virtualization of QD arrays [13, 14]. As an
503 open-source, extensible platform with comprehensive documentation, QDFlow is designed to
504 serve as both a research tool and a community resource.

505 QDFlow represents a paradigm shift among QD simulators. Whereas other simulations
506 typically rely on constant-capacitance models that impose static couplings regardless of de-
507 vice state, QDFlow ties these parameters directly to the underlying physics through its self-
508 consistent charge density, producing capacitances and observables that evolve dynamically
509 with gate voltages. This distinction not only improves the connection with the experiment but
510 also allows for the capture of nontrivial behaviors—such as QDs merging, fluctuating slopes,
511 and disorder-induced effects—that are inaccessible to static-capacitance approaches.

512 As QD systems advance toward larger arrays and integration into functional quantum pro-
513 cessors, the need for such realism will only grow. QDFlow package is currently being used
514 to generate datasets for multiple ongoing research projects and we intend to support it for
515 the foreseeable future. Although the current release is stable, we anticipate adding further
516 modules and functionality to the package. Possible future extensions of QDFlow, including
517 multi-dimensional modeling, adding additional quantum effects, hybridization with experi-
518 mental feedback loops, and systematic studies of robustness under different noise and dis-
519 order regimes, could establish it as a cornerstone for bridging theory, experiment, and ML
520 in the quest for scalable quantum technologies. We have designed the core class structure
521 to allow for seamless addition of new physical parameters and functions, and plan to update
522 the `generate` module to provide support for parallelization. By releasing QDFlow as an open-
523 source package, we aim to foster a shared foundation for accelerating progress in quantum dot
524 technologies. We anticipate that the package will not only continue to advance automated QD
525 control but also provide a flexible testbed for exploring broader questions at the intersection
526 of condensed matter physics, quantum information, and machine learning.

527 **Acknowledgements**

528 **Funding information** D.B. was supported in part by an ARO grant no. W911NF-24-2-0043.
529 S.S.K. acknowledges financial support from the S.N. Bose Fellowship during this project. This
530 research was performed in part while J.Z. held an NRC Research Associateship award at NIST.
531 The views and conclusions contained in this paper are those of the authors and should not be
532 interpreted as representing the official policies, either expressed or implied, of the U.S. Govern-
533 ment. The U.S. Government is authorized to reproduce and distribute reprints for Government
534 purposes, notwithstanding any copyright noted herein. Any mention of commercial products
535 is for information only; it does not imply recommendation or endorsement by NIST.

536 **Code availability** QDFlow is available on the [Python Package Index](#), with the source code
537 released under the GNU General Public License, and can be installed using `pip install`
538 `QDFlow` command. The associated GitHub repository is [https://github.com/QDFlow/QDFlow-](https://github.com/QDFlow/QDFlow-solver)
539 [solver](https://github.com/QDFlow/QDFlow-solver). Documentation is available at <https://qdfow-sim.readthedocs.io/>. Any discovered
540 bugs should be reported using GitHub [issues](#). If you find this package useful, please star the
541 repository and cite this paper.

542 **References**

- 543 [1] G. Burkard, T. D. Ladd, A. Pan, J. M. Nichol and J. R. Petta, *Semiconductor spin qubits*,
544 *Rev. Mod. Phys.* **95**(2), 025003 (2023), doi:[10.1103/RevModPhys.95.025003](https://doi.org/10.1103/RevModPhys.95.025003).
- 545 [2] A. B. Mei, I. Milosavljevic, A. L. Simpson, V. A. Smetanka, C. P. Feeney, S. M. Seguin, S. D.
546 Ha, W. Ha and M. D. Reed, *Optimization of quantum-dot qubit fabrication via machine*
547 *learning*, *Appl. Phys. Lett.* **118**(20), 204001 (2021), doi:[10.1063/5.0040967](https://doi.org/10.1063/5.0040967).
- 548 [3] C. Shen, W. Zhan, K. Xin, M. Li, Z. Sun, H. Cong, C. Xu, J. Tang, Z. Wu, B. Xu,
549 Z. Wei, C. Xue *et al.*, *Machine-learning-assisted and real-time-feedback-controlled growth*
550 *of inas/gaas quantum dots*, *Nat. Commun.* **15**(1), 2724 (2024), doi:[10.1038/s41467-](https://doi.org/10.1038/s41467-024-47087-w)
551 [024-47087-w](https://doi.org/10.1038/s41467-024-47087-w).
- 552 [4] D. Schug, T. J. Kovach, M. A. Wolfe, J. Benson, S. Park, J. P. Dodson, J. Corrigan,
553 M. A. Eriksson and J. P. Zwolak, *Automation of quantum dot measurement analysis*
554 *via explainable machine learning*, *Mach. Learn.: Sci. Technol.* **6**(1), 015006 (2025),
555 doi:[10.1088/2632-2153/ada087](https://doi.org/10.1088/2632-2153/ada087).
- 556 [5] E. Corcione, F. Jakob, L. Wagner, R. Joos, A. Bisquerra, M. Schmidt, A. D. Wieck, A. Lud-
557 wig, M. Jetter, S. L. Portalupi, P. Michler and C. Tarín, *Machine learning enhanced evalua-*
558 *tion of semiconductor quantum dots*, *Sci. Rep.* **14**(1), 4154 (2024), doi:[10.1038/s41598-](https://doi.org/10.1038/s41598-024-54615-7)
559 [024-54615-7](https://doi.org/10.1038/s41598-024-54615-7).
- 560 [6] J. D. Teske, S. S. Humpohl, R. Otten, P. Bethke, P. Cerfontaine, J. Dedden, A. Ludwig, A. D.
561 Wieck and H. Bluhm, *A machine learning approach for automated fine-tuning of semicon-*
562 *ductor spin qubits*, *Appl. Phys. Lett.* **114**(13), 133102 (2019), doi:[10.1063/1.5088412](https://doi.org/10.1063/1.5088412).
- 563 [7] R. Durrer, B. Kratochwil, J. Koski, A. Landig, C. Reichl, W. Wegscheider, T. Ihn and E. Gre-
564 plova, *Automated tuning of double quantum dots into specific charge states using neural net-*
565 *works*, *Phys. Rev. Appl.* **13**(5), 054019 (2020), doi:[10.1103/PhysRevApplied.13.054019](https://doi.org/10.1103/PhysRevApplied.13.054019).

- 566 [8] J. Darulová, S. J. Pauka, N. Wiebe, K. W. Chan, G. C. Gardener, M. J. Manfra, M. C. Cassidy
567 and M. Troyer, *Autonomous tuning and charge-state detection of gate-defined quantum dots*,
568 Phys. Rev. Appl. **13**(5), 054005 (2020), doi:[10.1103/PhysRevApplied.13.054005](https://doi.org/10.1103/PhysRevApplied.13.054005).
- 569 [9] J. P. Zwolak, T. McJunkin, S. S. Kalantre, J. Dodson, E. R. MacQuarrie, D. Savage,
570 M. Lagally, S. Coppersmith, M. A. Eriksson and J. M. Taylor, *Autotuning of double-*
571 *dot devices in situ with machine learning*, Phys. Rev. Appl. **13**(3), 034075 (2020),
572 doi:[10.1103/PhysRevApplied.13.034075](https://doi.org/10.1103/PhysRevApplied.13.034075).
- 573 [10] N. M. van Esbroeck, D. T. Lennon, H. Moon, V. Nguyen, F. Vigneau, L. C. Camenzind,
574 L. Yu, D. M. Zumbühl, G. A. D. Briggs, D. Sejdinovic and N. Ares, *Quantum device*
575 *fine-tuning using unsupervised embedding learning*, New J. Phys. **22**(9), 095003 (2020),
576 doi:[10.1088/1367-2630/abb64c](https://doi.org/10.1088/1367-2630/abb64c).
- 577 [11] H. Moon, D. T. Lennon, J. Kirkpatrick, N. M. van Esbroeck, L. C. Camenzind, L. Yu,
578 F. Vigneau, D. M. Zumbühl, G. A. D. Briggs, M. A. Osborne, D. Sejdinovic, E. A. Laird
579 *et al.*, *Machine learning enables completely automatic tuning of a quantum device faster*
580 *than human experts*, Nat. Commun. **11**(1), 4161 (2020), doi:[10.1038/s41467-020-](https://doi.org/10.1038/s41467-020-17835-9)
581 [17835-9](https://doi.org/10.1038/s41467-020-17835-9).
- 582 [12] J. P. Zwolak, T. McJunkin, S. S. Kalantre, S. F. Neyens, E. R. MacQuarrie, M. A. Eriksson
583 and J. M. Taylor, *Ray-based framework for state identification in quantum dot devices*, PRX
584 Quantum **2**(2), 020335 (2021), doi:[10.1103/PRXQuantum.2.020335](https://doi.org/10.1103/PRXQuantum.2.020335).
- 585 [13] J. Ziegler, F. Luthi, M. Ramsey, F. Borjans, G. Zheng and J. P. Zwolak, *Tuning arrays*
586 *with rays: Physics-informed tuning of quantum dot charge states*, Phys. Rev. Appl. **20**(3),
587 034067 (2023), doi:[10.1103/PhysRevApplied.20.034067](https://doi.org/10.1103/PhysRevApplied.20.034067).
- 588 [14] A. S. Rao, D. Buterakos, B. van Straaten, V. John, C. X. Yu, S. D. Oosterhout, L. Stehouwer,
589 G. Scappucci, M. Veldhorst, F. Borsoi and J. P. Zwolak, *Modular Autonomous Virtualiza-*
590 *tion System for Two-Dimensional Semiconductor Quantum Dot Array*, Phys. Rev. X **15**(2),
591 021034 (2025), doi:[10.1103/PhysRevX.15.021034](https://doi.org/10.1103/PhysRevX.15.021034).
- 592 [15] G. A. Oakes, J. Duan, J. J. L. Morton, A. Lee, C. G. Smith and M. F. G. Zalba, *Auto-*
593 *matic virtual voltage extraction of a 2x2 array of quantum dots with machine learning*,
594 doi:[10.48550/arXiv.2012.03685](https://doi.org/10.48550/arXiv.2012.03685) (2024).
- 595 [16] J. P. Zwolak, J. M. Taylor, R. W. Andrews, J. Benson, G. W. Bryant, D. Buterakos, A. Chat-
596 terjee, S. Das Sarma, M. Eriksson, E. Greplová, M. J. Gullans, F. Hader *et al.*, *Data needs*
597 *and challenges for quantum dot devices automation*, npj Quantum Inf. **10**(1), 105 (2024),
598 doi:[10.1038/s41534-024-00878-x](https://doi.org/10.1038/s41534-024-00878-x).
- 599 [17] V. Gualtieri, C. Renshaw-Whitman, V. Hernandez and E. Greplova, *Qdsim: A user-friendly*
600 *toolbox for simulating large-scale quantum dot devices*, SciPost Phys. Codebases p. 46
601 (2025), doi:[10.21468/SciPostPhysCodeb.46](https://doi.org/10.21468/SciPostPhysCodeb.46).
- 602 [18] B. van Straaten, J. Hickie, L. Schorling, J. Schuff, F. Fedele and N. Ares, *Qarray: A gpu-*
603 *accelerated constant capacitance model simulator for large quantum dot arrays*, SciPost
604 Phys. Codebases p. 35 (2024), doi:[10.21468/SciPostPhysCodeb.35](https://doi.org/10.21468/SciPostPhysCodeb.35).
- 605 [19] J. A. Krzywda, W. Liu, E. van Nieuwenburg and O. Krause, *QDarts: A quantum dot array*
606 *transition simulator for finding charge transitions in the presence of finite tunnel couplings,*
607 *non-constant charging energies and sensor dots*, SciPost Phys. Codebases p. 43 (2025),
608 doi:[10.21468/SciPostPhysCodeb.43](https://doi.org/10.21468/SciPostPhysCodeb.43).

- 609 [20] S. S. Kalantre, J. P. Zwolak, S. Ragole, X. Wu, N. M. Zimmerman, M. D. Stewart and J. M.
610 Taylor, *Machine learning techniques for state recognition and auto-tuning in quantum dots*,
611 npj Quantum Inf. **5**(1), 6 (2019), doi:[10.1038/s41534-018-0118-7](https://doi.org/10.1038/s41534-018-0118-7).
- 612 [21] J. P. Zwolak, S. S. Kalantre, X. Wu, S. Ragole and J. M. Taylor, *QFlow lite dataset: A*
613 *machine-learning approach to the charge states in quantum dot experiments*, PLoS ONE
614 **13**(10), e0205844 (2018), doi:[10.1371/journal.pone.0205844](https://doi.org/10.1371/journal.pone.0205844).
- 615 [22] National Institute of Standards and Technology, *Qflow 2.0: Quantum dot data for machine*
616 *learning*, Database: data.nist.gov, <https://doi.org/10.18434/T4/1423788> (2022).
- 617 [23] A. Zubchenko, D. Middlebrooks, T. Rasmussen, L. Lausen, F. Kuemmeth, A. Chatterjee
618 and J. P. Zwolak, *Autonomous bootstrapping of quantum dot devices*, Phys. Rev. Appl.
619 **23**(1), 014072 (2025), doi:[10.1103/PhysRevApplied.23.014072](https://doi.org/10.1103/PhysRevApplied.23.014072).
- 620 [24] J. P. Zwolak, S. S. Kalantre, T. McJunkin, B. J. Weber and J. M. Taylor, *Ray-based classifi-*
621 *cation framework for high-dimensional data*, In *Third Workshop on Machine Learning and*
622 *the Physical Sciences (NeurIPS 2020)*, pp. 1–7. Vancouver, Canada, ArXiv:2010.00500
623 (2020).
- 624 [25] J. Ziegler, T. McJunkin, E. S. Joseph, S. S. Kalantre, B. Harpt, D. E. Savage,
625 M. G. Lagally, M. A. Eriksson, J. M. Taylor and J. P. Zwolak, *Toward robust au-*
626 *totuning of noisy quantum dot devices*, Phys. Rev. Appl. **17**(2), 024069 (2022),
627 doi:[10.1103/PhysRevApplied.17.024069](https://doi.org/10.1103/PhysRevApplied.17.024069).
- 628 [26] D. L. Buterakos, S. S. Kalantre, J. Ziegler, J. M. Taylor and J. P. Zwolak, *QDFlow: A Python*
629 *package for physics simulations of quantum dot devices*, GitHub (2025).
- 630 [27] O. Ciftja, *Electrostatic interaction energy between two coaxial parallel uniformly charged*
631 *disks*, Results Phys. **15**, 102684 (2019), doi:[10.1016/j.rinp.2019.102684](https://doi.org/10.1016/j.rinp.2019.102684).
- 632 [28] A. Alexandradinata, N. P. Armitage, A. Baydin, W. Bi, Y. Cao, H. J. Changlani, E. Chertkov,
633 E. H. da Silva Neto, L. Delacretaz, I. E. Baggari, G. M. Ferguson, W. J. Gannon *et al.*,
634 *The future of the correlated electron problem*, SciPost Phys. Comm. Rep. p. 8 (2025),
635 doi:[10.21468/SciPostPhysCommRep.8](https://doi.org/10.21468/SciPostPhysCommRep.8).
- 636 [29] J. Darulová, M. Troyer and M. C. Cassidy, *Evaluation of synthetic and experimental train-*
637 *ing data in supervised machine learning applied to charge-state detection of quantum dots*,
638 Mach. Learn.: Sci. Technol. **2**(4), 045023 (2021), doi:[10.1088/2632-2153/ac104c](https://doi.org/10.1088/2632-2153/ac104c).
- 639 [30] C. W. J. Beenakker, *Theory of coulomb-blockade oscillations in the conductance of a quan-*
640 *tum dot*, Phys. Rev. B **44**, 1646 (1991), doi:[10.1103/PhysRevB.44.1646](https://doi.org/10.1103/PhysRevB.44.1646).
- 641 [31] J. Ziegler, F. Luthi, M. Ramsey, F. Borjans, G. Zheng and J. P. Zwolak, *Automated extraction*
642 *of capacitive coupling for quantum dot systems*, Phys. Rev. Appl. **19**(5), 054077 (2023),
643 doi:[10.1103/PhysRevApplied.19.054077](https://doi.org/10.1103/PhysRevApplied.19.054077).